Acta Geotechnica
https://doi.org/10.1007/s11440-025-02835-0

RESEARCH PAPER

Behaviour of GFRP-confined sand and cemented sand under four-point flexural tests

Jing-Cheng Teng[1,2,3,4] · Wen-Bo Chen[1,2] · Ding-Bao Song[4] · Yin-Fu Jin[1,2,3] · Zhen-Yu Yin[4] · Jian-Guo Dai[5] · Xiang-Sheng Chen[1,2,3]

Received: 26 May 2025 / Accepted: 24 October 2025

Abstract

The use of fibre-reinforced polymer (FRP) composites is on the rise due to their excellent corrosion resistance, making them a viable alternative to traditional piling materials in harsh environments. This paper presents a new glass fibre-reinforced polymer (GFRP) pile that includes an outer GFRP tube filled with sand or cemented sand. Four-point flexural tests are conducted to evaluate the flexural behaviour of the new pile, and the Optical Frequency Domain Reflectometry (OFDR) technique is utilized to capture the longitudinal strain distributions during the tests. The effects of the type of infill material (sand, cemented sand, and fibre-reinforced cemented sand) and the thickness of the GFRP tube (3 mm, 5 mm) are investigated. All experimental results show a significant improvement in the flexural bearing capacity and ductility of the new pile structures compared to the hollow GFRP pile, which can be attributed to the presence of the infill materials. With the increase in the strength of the infill material, the stiffness and strength of the pile increase. The composite action of the ductile FRP composites and the high-ductile infill materials provides enhanced structural performance. A theoretical model is adopted to rationally predict the load–strain behaviour of GFRP-confined cemented sand piles.

Keywords Fiber-reinforced polymer · Flexural strength · Optical frequency domain reflectometry · Pile · Sand

Abbreviations

A_c	Cross-sectional area of cemented sand core
A_{FRP}	Cross-sectional area of FRP tube
C_c	Cement content
C_u	Coefficient of uniformity
D	Outer diameter of the FRP tube
d_{50}	Mean grain size
D_r	Relative density
e	Relative density
E	Elastic modulus
E_{ten}	Tensile elastic modulus
E_{com}	Compressive strength of FRP tube
E_c	Elastic modulus of cemented sand core
f_{co}	Compressive strength of the cemented sand core
f_{cu}	Compressive strength of FRP tube
$f_{cu(\text{Ten.})}$	Tensile strength of FRP tube

✉ Zhen-Yu Yin
zhenyu.yin@polyu.edu.hk

Jing-Cheng Teng
jingcheng.teng@szu.edu.cn

Wen-Bo Chen
geocwb@gmail.com

Ding-Bao Song
dingbao.song@polyu.edu.hk

Yin-Fu Jin
yinfujin@szu.edu.cn

Jian-Guo Dai
jiangdai@cityu.edu.hk

Xiang-Sheng Chen
xschen@szu.edu.cn

[1] The College of Civil and Transportation Engineering, Shenzhen University, Shenzhen, China

[2] State Key Laboratory of Intelligent Geotechnics and Tunnelling, Shenzhen University, Shenzhen, China

[3] National Engineering Research Center of Deep Shaft Construction, Shenzhen University, Shenzhen, China

[4] Department of Civil and Environmental Engineering, The Hong Kong Polytechnic University, Hung Hom, Kowloon, Hong Kong, China

[5] Department of Architecture and Civil Engineering, City University of Hong Kong, Kowloon, Hong Kong, China

Published online: 17 November 2025

$f_{cu(\mathrm{Com.})}$	Compressive strength of FRP tube
FC	Fibre content
f_{to}	Tensile strength of cemented sand core
G_s	Specific gravity of solids
I_e	Moment of inertia
M	Moment capacity
m_{sand}	Mass of the infill sand
m_{solid}	Mass of the infill
t	Deviatoric stress
q	Thickness
σ_c	Compressive strength of the confined cemented sand
σ_t	Tensile strength of the confined cemented sand
ε_a	Axial strain
ε_c	Compressive strain
ε_{co}	The corresponding compressive strain of the cemented sand at the peak point
ε_t	Tensile strain
ε_{to}	The corresponding tensile strain of the cemented sand at the peak point
ρ_{max}	Maximum dry density
ρ_{min}	Minimum dry density
ρ_{solid}	Density of the infill
$\theta_{\mathrm{winding}}$	Winding angle of the fibres
ξ	Confinement effect coefficient

1 Introduction

Foundation engineering often involves the use of concrete, steel, wood, or a combination of these materials. However, these traditional materials are prone to deterioration over time, particularly in marine environments. Infrastructure degradation not only results in significant maintenance costs but also poses severe safety hazards to both the infrastructure and its surrounding environment [1–3]. Fibre-reinforced polymer (FRP) possesses excellent corrosion resistance, thermal stability, lightweight construction, satisfactory strength, and high cost-effectiveness. As such, it has become a suitable substitute for conventional building materials in extreme environments [3–5].

The hybrid system for concrete-filled FRP tubes has proven to be highly effective in underground and marine environments [6–13], where applications include piles, retaining walls, and bridge components. The FRP tube serves as a casting mould for the new concrete while acting as a reinforced shell for corrosion resistance, thus streamlining and expediting the construction process. The FRP tube confines the concrete core, which in turn provides the tubes with internal support and resistance in the compression zone, thereby increasing the strength and ductility of the flexural members [14, 15]. Prestressed GFRP tubes filled with concrete were suggested for use as marine piles [16, 17], with different FRP sections spliced using short steel tubes. The conventional design of these structures has predominantly prioritized stiffness, often leading to insufficient utilization of material strength. To address these issues, various experimental studies have been conducted using FRP piles. Bending tests were carried out on hollow and concrete-filled Carbon fibre-reinforced polymer (CFRP) piles to examine the composite effect [18, 19]. Mirmiran A. et al. [20] investigated concrete-filled GFRP tubes in the form of piles and columns, and the study included two flexural tests to examine the effect of reinforcement on the wall thickness. The over-reinforced sections failed in compression at higher strength and lower deflection than under-reinforced sections. The hybrid FRP-concrete-steel double-skin tubular members [21] were proposed to provide additional shear resistance and higher flexural capacity. Hollow and concrete-filled pultruded GFRP tubes were studied by Ferdous et al. [22, 23] as modular retaining walls, and the study focused on the flexural performance of pultruded GFRP piles with square and circular cross-sections.

According to the reports by Ashpiz et al. [24], the utilization of the FRP composite seawall system may potentially eliminate the need for heavy machinery, resulting in a significant reduction in construction time when compared to conventional concrete seawalls. In practice, to ensure the stability of the pile, sand or cemented soil would be filled in the pile [25, 26] to satisfy relevant strength and deformation requirements. Recent research [27, 28] demonstrated, through three-point bending tests on cemented tailings backfill (CTB), that weakly cemented materials displayed good flexural resistance and ductility. Notably, the CTB had post-peak toughness even after reaching the peak load. These characteristics of weakly cemented materials, combined with the high-ductile FRP tubes, could have better composite effects on flexural behaviour. Yu et al. [29] and Zhao et al. [30] examined the mechanical properties of coal rejects-based backfill material (CBM) composed of coal rejects and cementitious grout materials confined by FRP tubes under compression tests. Teng et al. [31] investigated the compressive behaviour of FRP-confined sand and cemented sand columns. These findings revealed that the low-strength cemented infill material exhibited excellent load-bearing capacity and deformation capacity. However, these studies primarily concentrated on the compressive performance of FRP-confined low-strength cementitious material, while the exploration of its flexural behaviour was still limited.

In studies on FRP-confined low-strength materials, GFRP tubes have been predominantly employed. Compared with CFRP, GFRP exhibits a slightly lower elastic modulus but superior ductility. Teng et al. [31] demonstrated that, for weakly cemented materials, the use of an FRP jacket with excessively high stiffness can result in over-confinement, thereby diminishing the potential for material strengthening. On this basis, a new FRP tubular pile system that employs Fujian standard sand and cemented sand as infill materials was developed in this study. Using sand or cemented sand can reduce the use of cementitious grout material and correspondingly reduce the cost towards carbon neutrality. The flexural behaviour of its hybrid system was systematically studied through four-point bending tests consisting of 10 pile specimens. The test variables encompassed the thickness of the FRP tube (i.e. 3 mm and 5 mm) and the type of infill materials (i.e. sand, cemented sand, and fibre-reinforced cemented sand). In addition, the Optical Frequency Domain Reflectometry (OFDR) technique was utilized to measure the strain distribution in the middle section of the pile structures.

2 Experimental programme

2.1 Material properties

2.1.1 FRP composites

The FRP tubes used in this research were filament-wound E-glass FRP tubes, provided by Lianyungang Zhongfu Lianzhong Composites Group Co., Ltd., with two different thicknesses of 3 mm and 5 mm, designed to have the same volume fraction and winding angle. The GFRP tubes were oriented at ± 45° to the longitudinal axis, resulting in satisfactory stiffness in both hoop and axial directions. To assess the tensile properties of GFRP composites, 12 coupon specimens were cut from the GFRP tubes and subjected to tensile tests according to ASTM D3039 [32]. Compression tests on 8 short FRP tubes were also carried out following GB/T 5350–2005 [33]. The detailed properties of the GFRP material are listed in Table 1.

2.1.2 Sand

In this study, Fujian standard sand was used as the testing material. The sphericity of the sand particles was estimated, as shown in Fig. 1. The shape of the tested sand particles was predominantly spherical. The properties of the sand are summarized in Table 2, and the triaxial test results are shown in Fig. 2. All the testing sands could be classified as poorly graded sand (SP) according to ASTM D2487 [34]. The relative densities of all the sand samples used in this study were controlled at 90%.

2.1.3 Basalt fibre

Basalt fibre has excellent acid and alkali resistance, and mechanical properties, as shown in Table 3. Therefore, the 18-mm-long basalt fibres were mixed into the cemented sand samples with the intention of enhancing their tensile strength and ductility.

2.1.4 Cemented sand

In this study, cylindrical cemented sand samples with a 50 mm diameter and a 100 mm height were fabricated for conducting unconfined compression tests aimed at obtaining the material properties. Ordinary Portland cement (OPC) was employed for the preparation of the testing specimens. The masses of the cement and basalt fibres were determined based on the dry sand mass. This research investigated three different types of cemented sand samples, including samples with a 5% cement content (CC = 5%), samples with a 10% cement content (CC = 10%), and 1% basalt fibre-reinforced samples with a 5% cement content (FC = 1% and CC = 5%). Since the specific gravity of cement grains (3.15) surpasses that of sand particles, a composite specific gravity that takes into account the sand and cement content was adopted for void ratio calculations [35].

The sand and cement were mixed until a uniform mixture was obtained, following which water was added to generate a homogeneous paste. For the fibre-reinforced cemented sand, basalt fibres were added after the formation

Table 1 Properties of GFRP pile

Material type	Thickness (mm)	Fibre/matrix	E_{Ten} (GPa)		f_{tu} (Ten.) (MPa)		E_{Com} (GPa)		f_{cu} (Com.) (MPa)		$\theta_{winding}$ (°)
			Ave	S.D	Ave	S.D	Ave	S.D	Ave	S.D	
GFRP	3 5	E-glass/ Diglycidylether of bisphenol A resin	10.00	0.63	65.08	1.92	12.00	0.48	121.06	10.36	± 45

Ave. = average value; S.D. = standard deviation; E_{Ten} = Tensile elastic modulus; $f_{cu(\text{Ten.})}$ = ultimate tensile strength; E_{Com} = Compressive elastic modulus; $f_{cu(\text{Com.})}$ = ultimate compressive strength; $\theta_{winding}$ = winding angle of the fibres

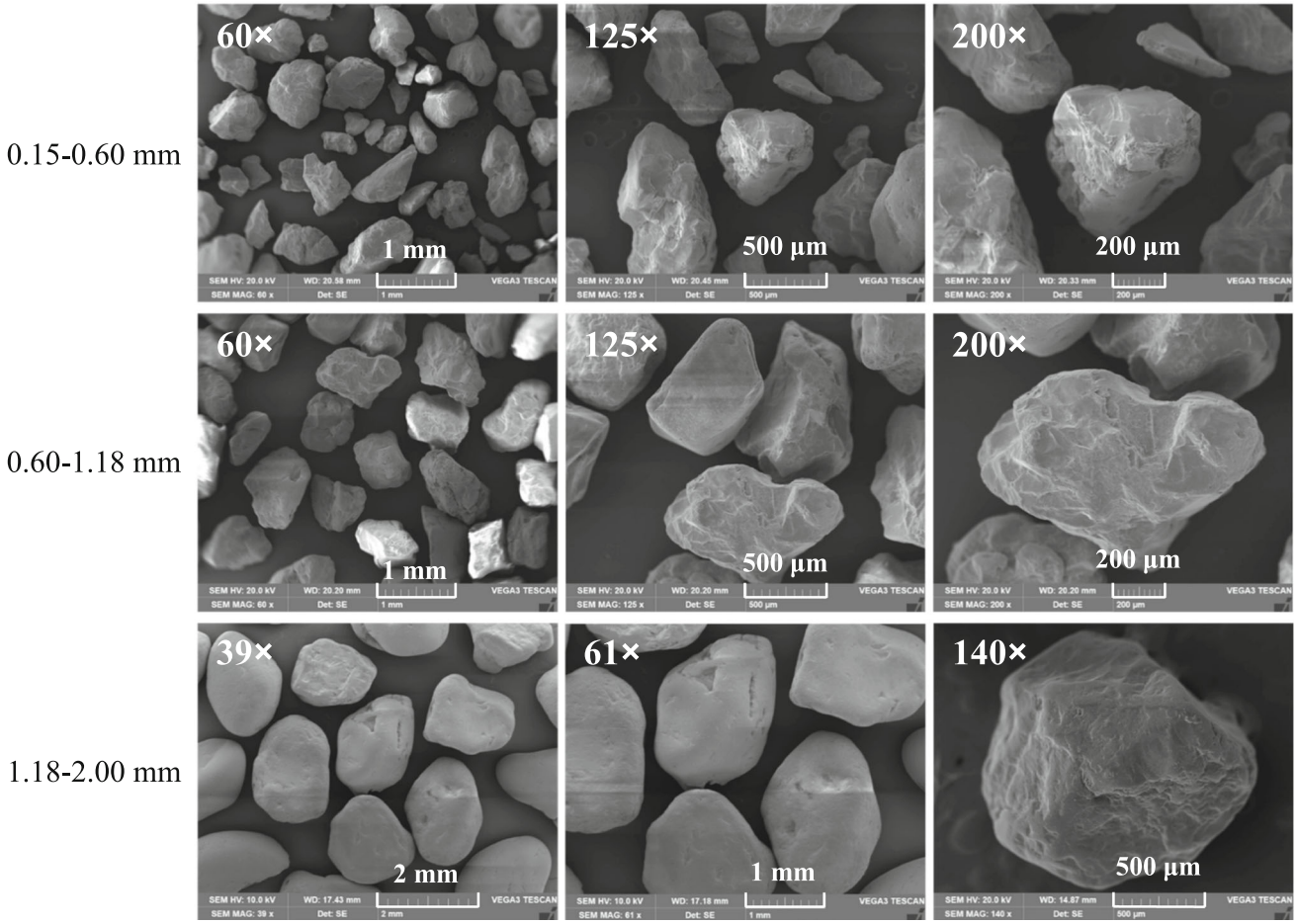

Fig. 1 SEM images of sand particles

Table 2 Physical properties of sand

Property	Value
Specific gravity, G_s	2.67
Maximum dry density, ρ_{max} (g/cm^3)	1.884
Minimum dry density, ρ_{min} (g/cm^3)	1.625
Mean grain size, d_{50} (mm)	0.83
Coefficient of uniformity, C_u	5.21

of a homogeneous paste, so as to avoid the formation of fibre clumps and floating. Following the moulding process, the samples were cured for 28 days at 23 °C ± 2 °C and relative humidity above 95% in a humid environment.

A series of unconfined compression tests (Fig. 3(a)) were conducted on the cemented sand sample according to the Brazilian standard NBR 5739 [36] to obtain its material properties, as illustrated in Fig. 3(b). Both the 5CS samples and 1F-5CS samples demonstrated an unconfined compression strength of 2 MPa, with ultimate strains of around 1.25% and 2.25%, respectively. The unconfined compression strength of the 10CS sample was around 7 MPa, and the ultimate strain was around 1.00%. The unconfined compression (UC) test results indicated that the strength of the cemented sand increased notably with the cement content. However, the inclusion of basalt fibre had a minor influence on the strength of the cemented sand but enhanced the ductility, which was consistent with the previous research [37, 38].

2.1.5 Test programme

In this research, a total of 10 specimens were prepared, comprising 2 hollow and 8 solid FRP tubes, which were categorized into two groups, as presented in Table 4. The aspect ratio of all specimens was adjusted to 11.2:1 with an inner diameter of 125 mm and a height of 1400 mm. The detailed information on the infill is listed in Table 5. For reference purposes, each specimen was assigned a name, beginning with 'M3' or 'M5' representing the tests with different FRP thicknesses, followed by a capital letter 'H', 'S', 'CS', or 'FCS', denoting the infill materials (i.e.

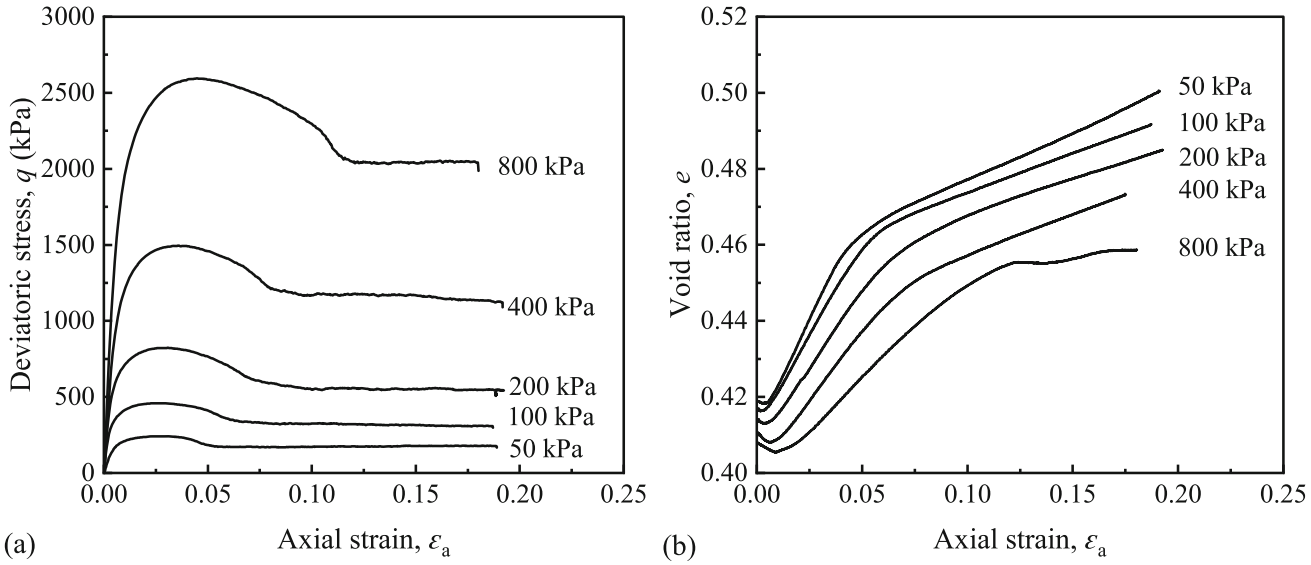

Fig. 2 **a** Deviatoric stress–axial strain relationship, and **b** void ratio–axial strain relationship of the sand sample

Table 3 Properties of basalt fibre

Parameters	Values
Density (g/cm^3)	2.63
Diameter (μm)	6–19
Tensile strength (MPa)	≥ 3000
Elastic modulus (GPa)	≥ 85

hollow pile, sand-filled FRP pile, cemented sand-filled FRP pile, and fibre-reinforced cemented sand-filled FRP pile). The numbers '5' and '10' preceding 'CS' indicate the cement content of the cemented sand.

The preparation process of the specimens involved the following steps: (1) sieving the sand to collect particles with a diameter ranging from 0.15 mm to 2 mm; (2) filling the hollow GFRP tube with sand and cemented sand followed by compacting the infill materials in ten layers statically to achieve the desired initial void ratio; (3) using aluminium caps to seal the ends of the piles; and (4) covering the prepared specimens with cling wrap to prevent moisture loss. In the case of sand-filled FRP tubes, the sand was compacted to a relative density of 90% (Dr = 90%). The weights and void ratios of sand and cemented sand were kept as closely matched as possible to ensure similar compactness levels.

2.1.6 Test setup and instrumentation

The flexural tests were conducted using a 20-t loading frame, with the test setup and sensor placement illustrated

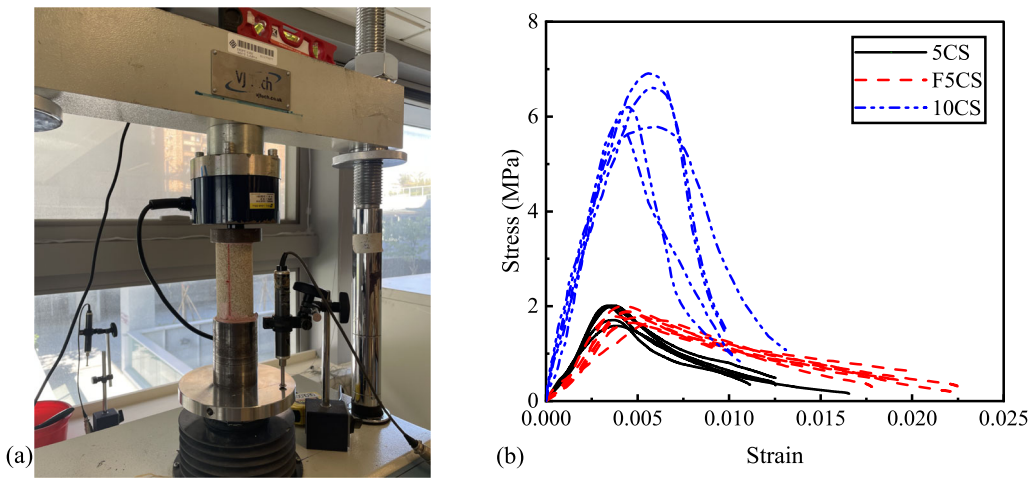

Fig. 3 **a** Setup of the unconfined compression test; and **b** stress–strain relationship of cemented sand with or without basalt fibre

Table 4 Test programme

Groups	Infill	Specimen	Ultimate load (kN)	t (mm)
A	Hollow tube	M3-H	20.00	3
	Sand (D_r = 90%)	M3-S	32.37	
	CC = 5%	M3-5CS	41.45	
	CC = 10%	M3-10CS	45.98	
	FC = 1% & CC = 5%	M3-F5CS	41.75	
B	Hollow tube	M5-H	37.01	5
	Sand (D_r = 90%)	M5-S	44.57	
	CC = 5%	M5-5CS	59.02	
	CC = 10%	M5-10CS	66.24	
	FC = 1% & CC = 5%	M5-F5CS	59.28	

D_r = relative density

Table 5 Specimens properties

Parameters	Sand	5CS	10CS	F5CS
Mass of the infill sand, m_{sand} (kg)	32.37	27.60	27.23	27.47
Mass of the infill, m_{solid} (kg)	32.37	31.74	32.68	31.86
Density of the infill, ρ_{solid} (g/cm^3)	1.884	1.847	1.902	1.854^3
Void ratio, e (sand and cement)	0.42	0.45	0.43	0.45
Cement content (%)	0	5%	10%	5%
Fibre content (%)	0	0	0	1%
Water content (%)	0	10%	10%	10%

in Fig. 4. For each specimen, five axial strain gauges with a 20 mm gauge length were attached to the surface of the pile in the mid-section, while two strain rosettes were pasted at the midpoint of the shear span. Additionally, a pull rope displacement sensor (500 mm) was installed at the bottom of the middle position of the pile, and a 200-mm LVDT was placed at the top of the middle position of the pile, with two 50-mm LVDTs at the two-edge supporting points. All loads, displacements, and strains were automatically recorded by a data acquisition system.

To capture the axial strain distribution along the pile length, Optical Frequency Domain Reflectometry (OFDR) was employed in this study, which had a spatial resolution of 0.5 mm and an excellent measurement accuracy of ± 1 με. A 0.9 mm thick SMG.652b fibre with polyimide/HY coating was chosen as the sensing fibre, as it prevented fibre breakage in large-scale specimens. Four sections of OFDR fibres with 200 mm length and one 1200 mm OFDR fibre were uniformly distributed on the surface of the pile at the same heights as the five strain gauges, with the longest one placed at the bottom of the pile.

2.1.7 Experimental results and discussions

The following sections describe the test results and discussions, including the effects on pile thickness and the infill materials. It is worth noting that the weight, grain size distribution (GSD) and density of the infill materials were strictly controlled to maintain consistency during the preparation of the specimens. Under these conditions, the properties of sand, cemented sand, and FRP tubes remained relatively stable. Therefore, in this study, only a portion of the specimens was conducted with repeated tests to ensure the reliability of the results. To clearly present the structural performance in the subsequent figures, only one result from each sample group is displayed.

2.1.8 Behaviour of hollow piles

During the four-point flexural test, the hollow GFRP piles were ovalized due to the vertical component of the internal axial force acting on the section, which produced local lateral bending in the compression zone. The GFRP hollow

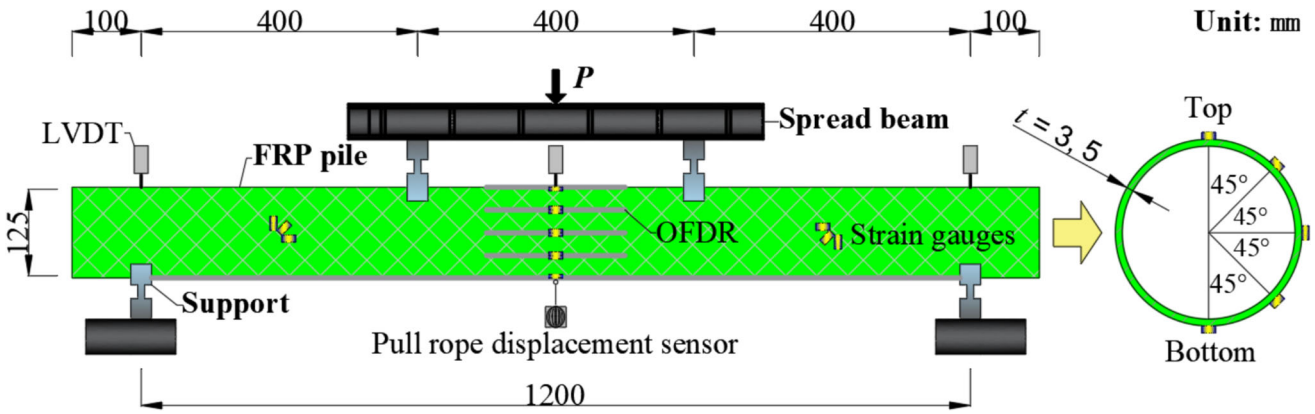

Fig. 4 Test setup and sensor placement

pile with a thickness of 3 mm experienced buckling failure in the compression zone after ovalization (Fig. 5(a)). However, the failure mode of the 5 mm thick GFRP hollow pile was the fibre rupture at the loading point, as shown in Fig. 5(b), which suggested that the resistance of the compression zone increased significantly as the thickness of the GFRP pile increased and the fibres in the tension zone broke first.

Figure 6 shows the test results of the hollow GFRP piles. All deflection and strain results are measured in the middle section of the specimens. The thicker pile demonstrated a significantly greater flexural capacity and ductility. During the loading process, a cracking sound was occasionally heard when the load–deflection curve reached the turning point, after which the load on the specimen gradually became stable. Analysis of the load–deflection curve (Fig. 6(a)) revealed that the 3 mm thick hollow FRP pile failed when the mid-span deflection exceeded 1/20 span (60 mm), while the 5 mm thick hollow FRP pile exhibited good ductility and did not fail until the mid-span deflection exceeded 1/10 span (120 mm) due to the increased compressive resistance at the compression zone. The deflection at the top of the mid-section of the 3 mm thick FRP tube was observed to be gradually larger than that at the bottom of the mid-section during the loading process, as illustrated in Fig. 6(a) and (b), suggesting the occurrence of buckling failure. In contrast, for the FRP tube with a 5 mm thickness, the top–bottom deflection difference was almost zero at the initial loading stage. However, after the load exceeded the yield load point, the deflection difference became apparent, indicating that buckling also occurred.

Figure 6(c) presents two typical compression–tensile strain curves for the two specimens, where the compressive and tensile strains were measured by two strain gauges located at the top and bottom of the mid-span, respectively. The smaller compressive strain of the thinner pile was attributed to the premature buckling of the compression zone. In both cases, the relationship of the compressive–tensile strain was initially linear. However, due to the influence of buckling in the compression zone, the increase in compressive strain for the 3 mm thick pile becomes less pronounced. Figure 6(d) describes the axial strain distributions, monitored by five strain gauges and OFDR, as shown in Fig. 4. The black curves represent the results of specimens with a wall thickness of 5 mm, while the red curves depict the results of specimens with a wall thickness of 3 mm. The change in the neutral axis depth during the test could be obtained from the axial strain distribution results. The position of the neutral axis was almost maintained at the centre of the cross-section due to the ovalization effect and the compressive buckling in the compression zone, until failure occurred after cracking in the tension zone. According to the axial strain profile monitored under multiple loading steps using OFDR technology in the hollow pile, a constant tensile strain region of 0.15 m was identified in the tension zone (Fig. 6(e)), which was confined within a range similar to that of the buckled area.

The moment of inertia (I_e) of the cross-section for the FRP pipe piles with thicknesses of 3 mm and 5 mm is 247 cm^4 and 432 cm^4, respectively. With a 75% increase in the moment of inertia of the hollow FRP pile, the ultimate bearing capacity increased by 85%, and the maximum deflection almost doubled. The moment of inertia and bearing capacity of the hollow section exhibited a roughly proportional increase. These findings implied that the greater thickness of the FRP hollow pile could improve the compressive capacity of its compression zone, thereby preventing premature buckling, and, in turn, increasing the

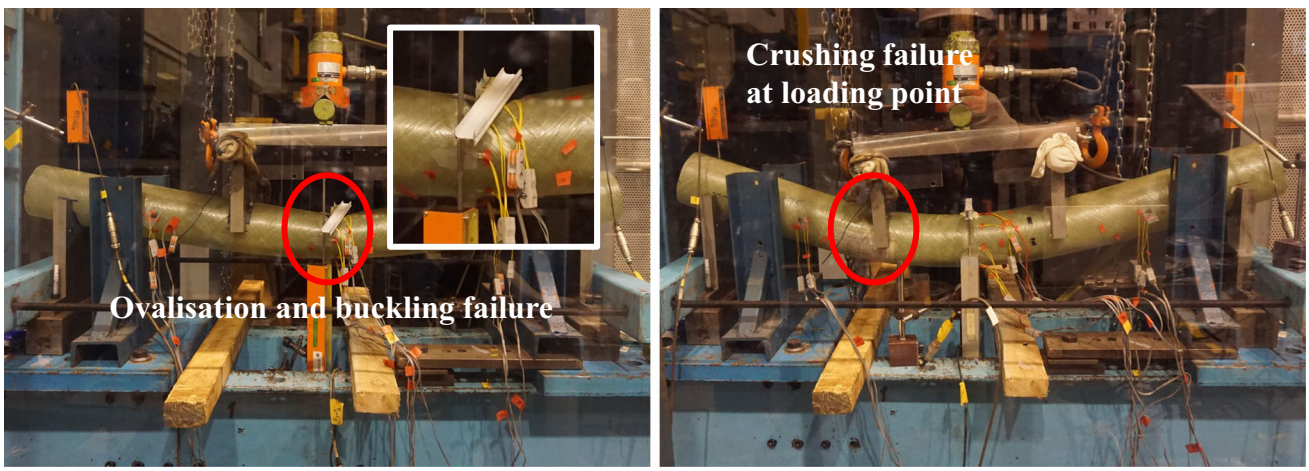

Fig. 5 Failure modes of GFRP hollow sections with **a** 3 mm thickness and **b** 5 mm thickness

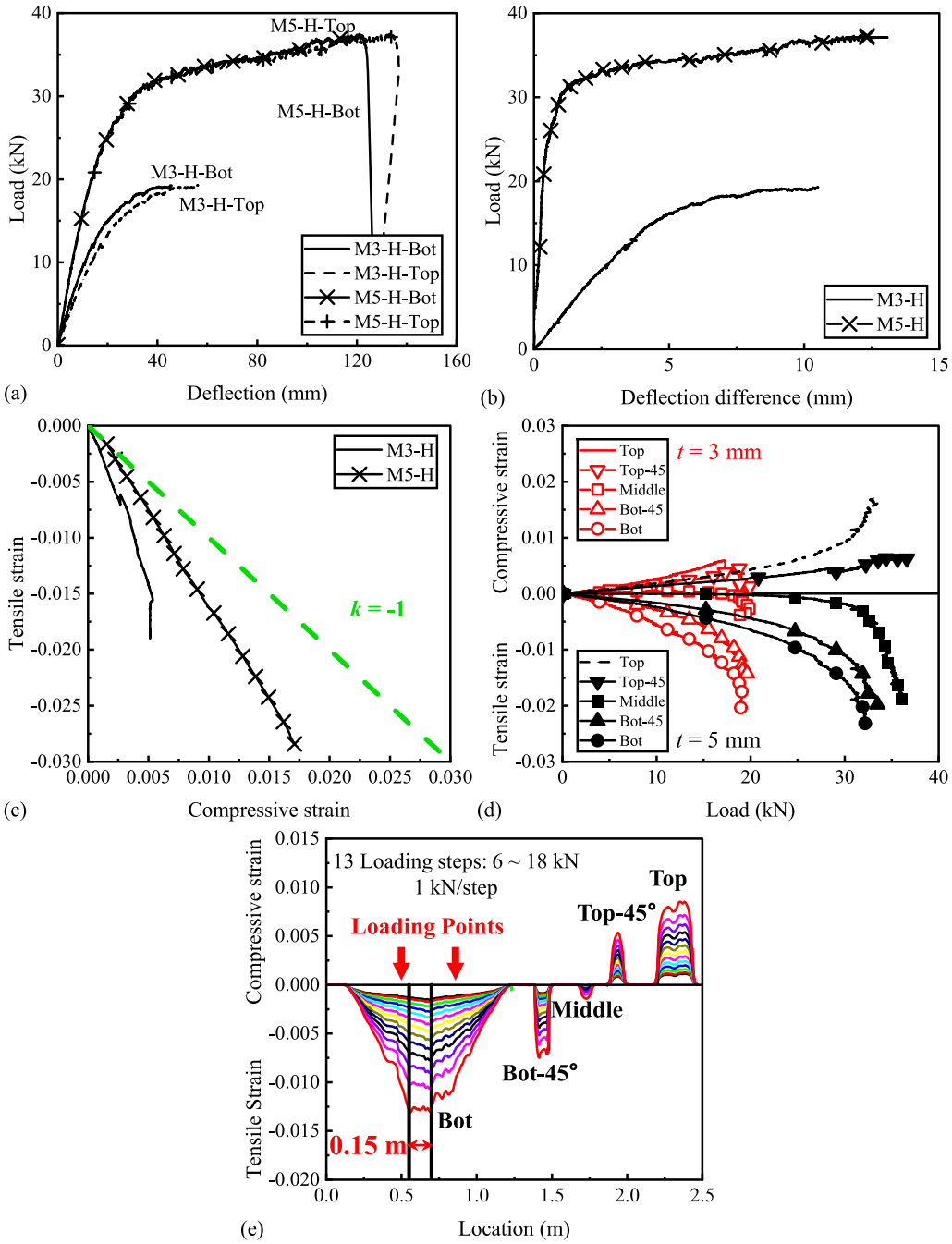

Fig. 6 Test results for hollow GFRP piles: **a** load–deflection relationships; **b** deflection difference from top and bottom points at the middle section; **c** tensile–compressive strain relationships; **d** axial strain distributions; and **e** typical strain profile

ductility and the flexural strength of the piles. However, it should be noted that the failure mode of the thicker hollow pile also involved buckling in the compression zone after reaching a certain degree of bending.

2.1.9 Behaviour of sand-filled FRP piles

The sand-filled FRP piles were fixed at both ends using aluminium caps during the test to prevent sand leakage, as depicted in Fig. 7. The thinner pile exhibited local crushing and splitting at the loading position due to the lack of strength in the hoop direction (Fig. 7 (a)), while the thicker pile experienced both compression and tension failure at the upper and lower sections of the loading position (Fig. 7 (b)).

Figure 8(a) depicts the effect of dense sand filling on the performance of GFRP piles. Upon reaching the ultimate load, distinct fracture sounds were observed, after which

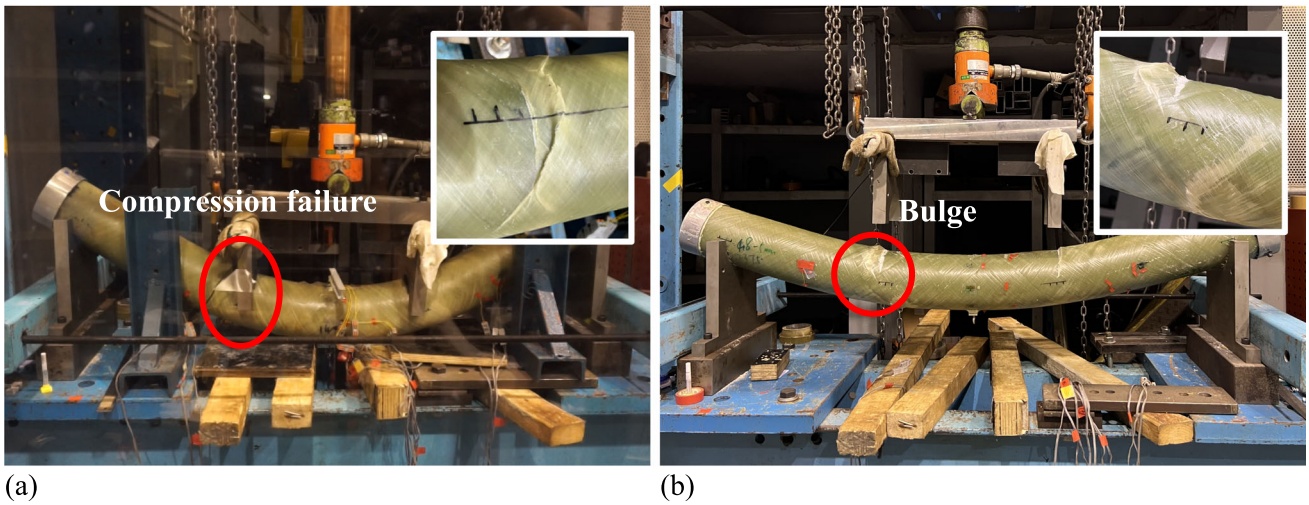

Fig. 7 Photograph of failure modes for sand-filled GFRP piles with **a** 3 mm thickness and **b** 5 mm thickness

the FRP pile underwent a distinctly brittle failure accompanied by an immediate loss of bearing capacity. The results show that the strength and stiffness of the sand-filled GFRP piles increased slightly, whereas the ductility improved significantly. The flexural strength of the sand-filled piles with thicknesses of 3 mm and 5 mm, increased by 61.85% (12.37 kN) and 20.43% (7.56 kN), respectively. Since the sand had no tensile capacity, the sand core had a minimal impact on the tension zone. Additionally, dense sand provided internal support for the GFRP tube, preventing ovalization and buckling in the compression zone, allowing the GFRP pile to maintain a gradually increasing flexural capacity after reaching the yield state. The top–bottom deflection difference of the sand-filled GFRP piles became minimal (Fig. 8(b)), and their compressive strain (Fig. 8(c)) was higher than that of hollow piles. It was worth noting that the values of the tensile strain and compressive strain were almost the same at the initial loading stages for the sand-filled pile. When combined with the result of axial strain distribution shown in Fig. 8(d), it could be observed that, due to the presence of the sand core, the stiffness of the compression zone of the pile was increased. This resulted in the depth of the neutral axis remaining nearly at the cross-sectional centre, until tensile cracking occurred, leading to failure and causing the movement of the neutral axis to balance the internal tension in the section. The presence of internal support from the sand core and the absence of buckling in the compression zone allowed for an expanded stable strain range (Fig. 8(e)) at the bottom (0.3 m), although it was slightly smaller than the loading interval (0.4 m).

The mid-span deflection of the sand-filled FRP piles exceeded 1/6 of the span (200 mm) at the end of the tests, white patches appeared below or close to the two load points, and other less prominent cracks were randomly distributed in the pure bending area. The thicker pile exhibited lower deformability, which was also the reason for its less pronounced strength enhancement. The thinner pile failed due to local crushing at the loading position, but the 5 mm thick pile had a higher compressive capacity, and thus, the infill sand at the loading position was squeezed, causing the pile wall to expand and bulge.

Following the flexural tests, the infill sand from the FRP pile was extracted by cutting the pile wall. The sand particles beneath the loading point and within the compression zone were separated from other sand particles, and subsequent sieving tests were conducted to determine the grain size distribution of the two parts of sand samples after the tests. As shown in Fig. 9, the GSD curve revealed that the compressed sand became more uniform compared to the initial GSD curve, whereas the GSD of the sand in other regions remained similar to the initial GSD curve. However, the GSD curves of specimens with different thicknesses were basically the same, which showed that the thickness of the pile had little effect on the particle breakage of the sand core. This phenomenon was due to the fact that the thickened pile wall was more involved in the buckling resistance of the compression zone, which can be obtained from the results of the hollow pile.

2.1.10 Behaviour of cemented sand-filled FRP piles

Despite the weaker strength of cemented sand compared to concrete, it exhibited superior ductility and primarily experienced shearing failure. The presence of the FRP jacket provided excellent shear resistance. These characteristics suggested that the FRP tube and cemented sand could work together almost throughout the test, resulting in piles with exceptional strength and ductility.

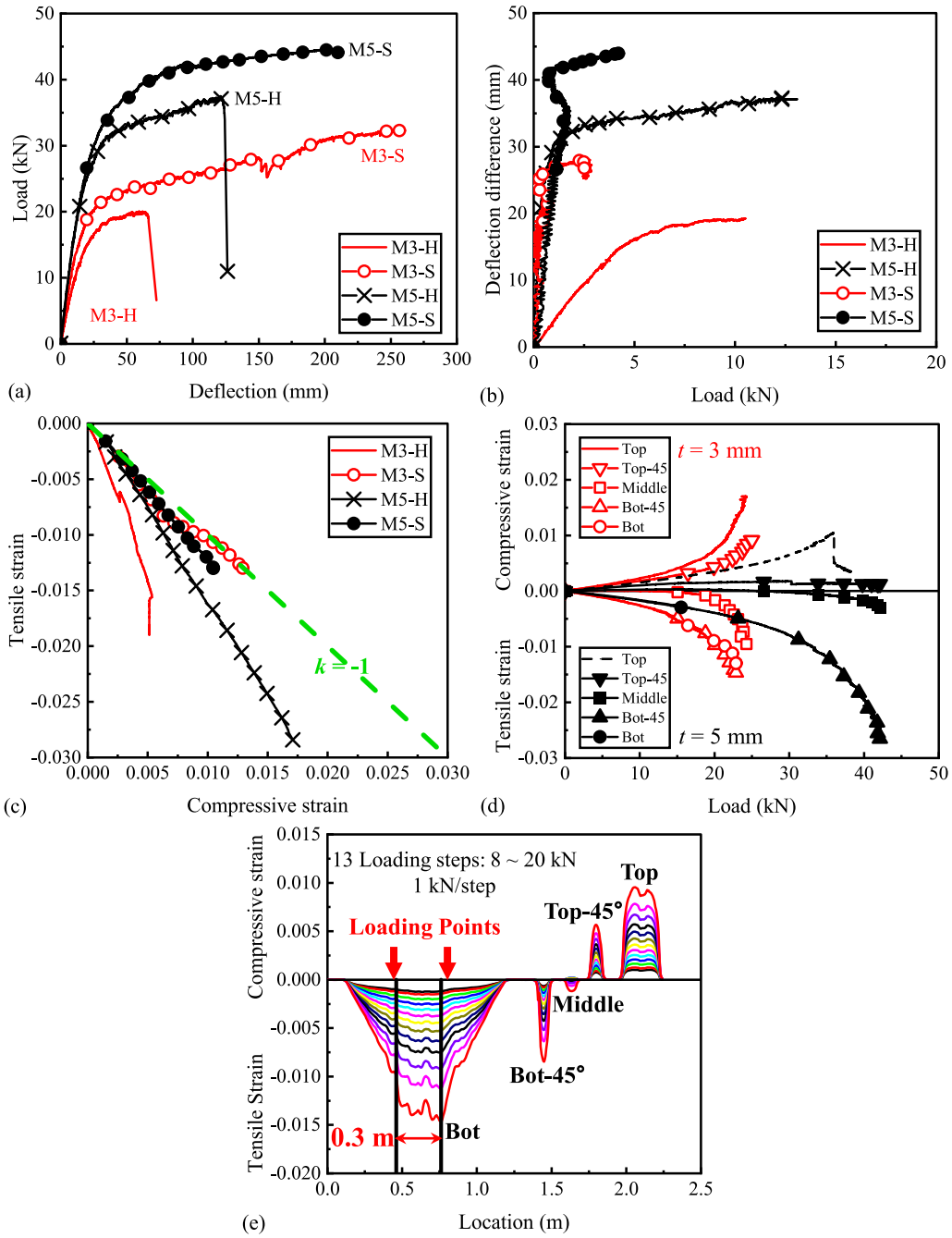

Fig. 8 Test results for sand-filled GFRP piles: **a** load–deflection relationships; **b** deflection difference from the top and bottom points at the middle section; **c** tensile–compressive strain relationships; **d** axial strain distribution; and **e** typical strain profile

After the test, for some specimens, the FRP shell was cut to expose the cemented sand core and examine the crack distribution. As illustrated in Fig. 10, cracks were observed along the length of the pile, and evident fracturing damage was observed at the loading points in the cemented sand. Moreover, some specimens exhibited oblique cracks in the shear span (Fig. 10(c)). The failure modes of the tested specimens are presented in Fig. 11. For FRP piles filled with cemented sand, flexural tension failure due to fibre rupture below the loading point and local crushing failure of the FRP tube at the loading point were the primary failure modes. The thicker FRP pile with 5 mm thickness had higher axial stiffness and experienced higher load, so the cemented sand at the loading point was subjected to greater pressure. Therefore, during the loading process, the cemented sand at the loading point was initially compressed and fractured. As the deflection increased, the bending at the loading point became more pronounced,

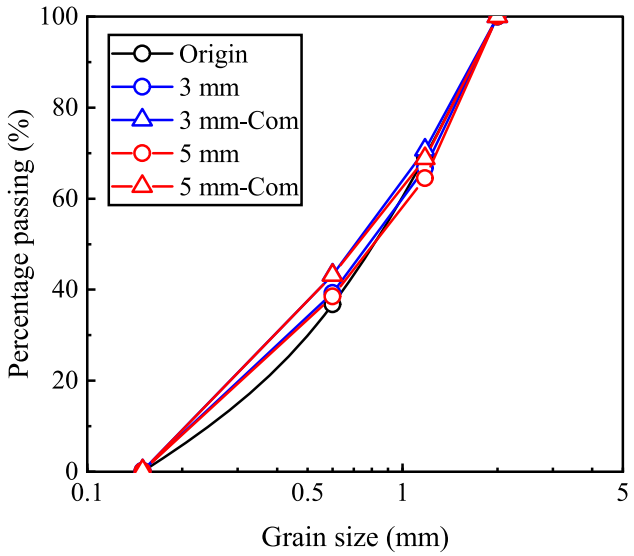

Fig. 9 Comparison of the grain size distribution of sand before and after the four-point flexural test

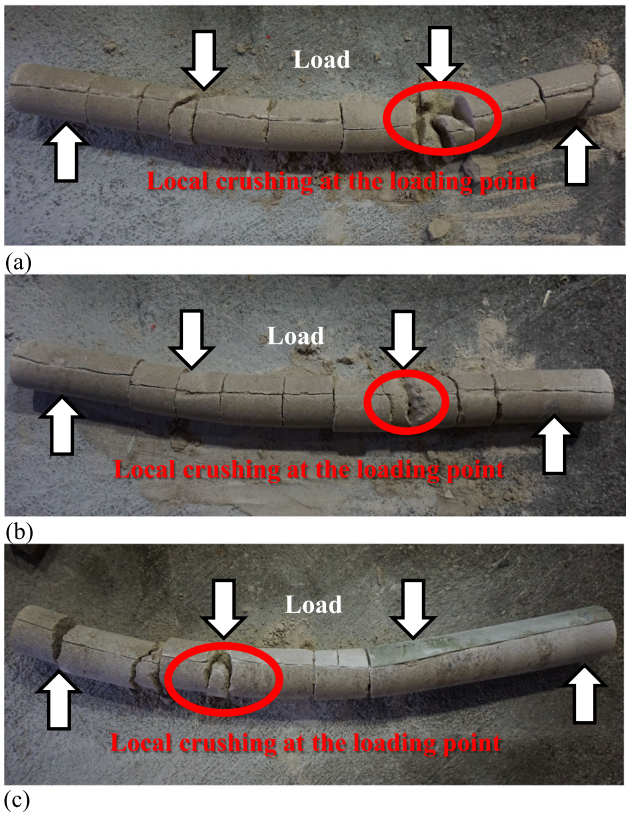

Fig. 10 Crack distribution of the cemented sand with **a** 5% cement content; **b** 1% basalt fibre and 5% cement content; and **c** 10% cement content

resulting in localized compression and the formation of a bulge. During this process, the composite action between the cemented sand and the GFRP tube was partially lost, resulting in a partial slippage between the cemented sand and the GFRP tube, causing a reduction in load transfer capacity. The slip was the most obvious for the cemented sand sample with 5% cement content (around 10 mm), while the sample with 10% cement content and the sample incorporated with basalt fibres had smaller slippage. This observation may be attributed to the high strength of the infill sample and the reinforcement ability of basalt fibres, respectively. For the thinner FRP pile with 3 mm thickness, no slip between the cemented sand and the FRP pile was observed due to the smaller axial stiffness.

The load–deflection relationships of all the specimens are shown in Fig. 12(a). The unconfined compressive strength of the cemented sand samples in this study was very low, ranging from 2 to 7 MPa, leading to a more pronounced effect of FRP confinement in terms of strength enhancement compared to the unconfined strength [31]. The tensile–compressive curve of all the specimens filled with cemented sand exhibited linearity, indicating that no obvious defects occurred on the piles within the gauge length. For the specimens of Group A with 3 mm thickness, the ultimate loads of the three FRP piles M3-5CS, M3-F5CS, and M3-10CS filled with cemented sand increased by 107.25% (21.45 kN), 108.75% (21.755 kN), and 122.90% (25.98 kN), respectively, compared to the hollow pile. A cemented sand core, compared to a pure sand core, possesses higher strength and stiffness, along with a certain tensile strength. Therefore, the cemented sand core provides a greater enhancement of both the strength and stiffness of GFRP piles compared to the sand core. However, shear and tensile failures that occurred in the cemented sand core could break the GFRP jacket, leading to a reduction in the ductility of GFRP piles. With the increase in cement content, the improvement of the pile flexural strength by the internally filled cemented sand sample was more significant. The sample mixed with basalt fibre only showed a small increase in the stiffness of the pile. During the test, many white patches appeared on the lower part of the FRP pile, indicating cracks in the cemented sand sample. When the mid-span deflection of the FRP pile exceeded 1/6 of the span and approached the ultimate state, fibre ruptures gradually occurred in the tension zone below the loading point.

For the specimens in Group B (t = 5 mm), the ultimate loads of M5-5CS, M5-F5CS, and M5-10CS were 59.47% (22.01 kN), 60.17% (22.27 kN), and 78.98% (29.23 kN) higher than the hollow pile, respectively. It is crucial to note that increasing the thickness of the GFRP tube had a more pronounced influence on pile strength, leading to a reduced proportion of strength enhancement. The load increments observed in Group B specimens were close to those in Group A specimens, owing to the considerably reduced ductility in Group B specimens (failure occurred when the mid-span deflection exceeded 1/8 of the span).

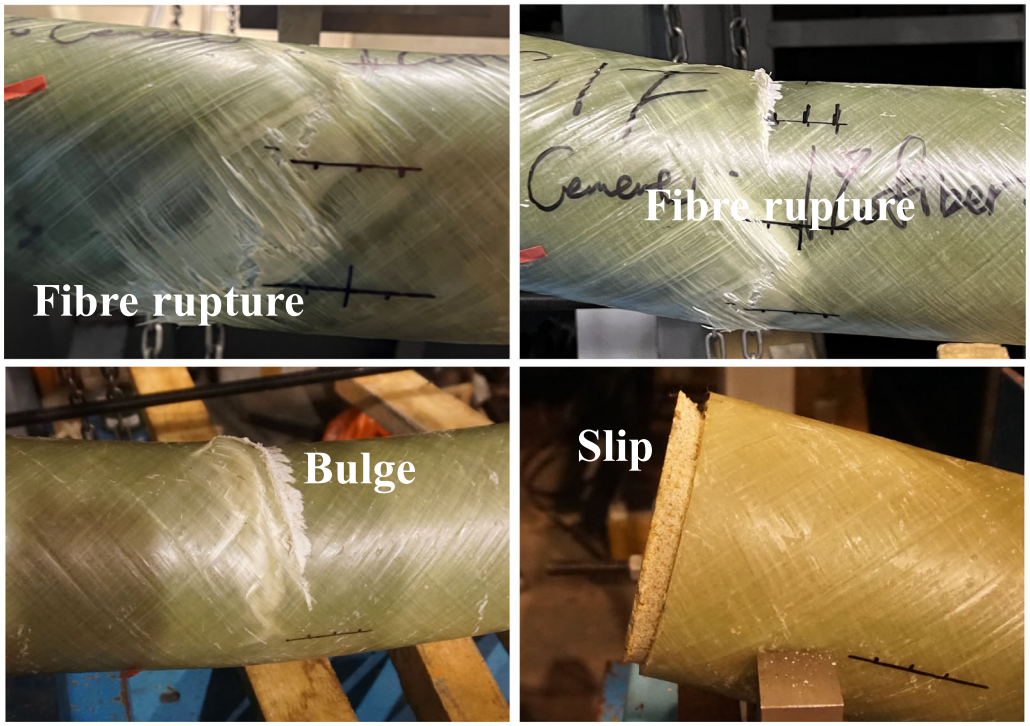

Fig. 11 Main failure modes of GFRP-confined cemented sand piles

Nevertheless, at a given deflection, the load increments in Group B were substantially higher than those in Group A, indicating that the larger thickness of the FRP tube exerted a more pronounced confinement effect on the cemented sand core, leading to an enhanced load capacity.

From Fig. 12(b), the tensile strain of the cemented sand-filled piles was significantly increased, and this elevation became more pronounced with the enhanced strength of the cemented sand core. This indicated the contribution of the cemented sand core in the tensile zone, resulting in a gradual shift of the neutral axis towards the compressive side from the initial loading stage, enabling a greater extent of synergistic deformation of 0.5 m in the bottom region.

2.1.11 Comparison with previous studies

By comparing with previous studies on GFRP-confined concrete piles, a more comprehensive evaluation of the performance of this new GFRP pile variant can be conducted. Ferdous et al. [22, 23] conducted four-point bending tests on concrete-filled FRP piles with a shear span/diameter ratio (3.10) similar to this study (3.05). The filling of concrete resulted in a 160.61% increase in the flexural strength of the FRP pile as illustrated in Table 6, only slightly higher than the load increments (122.90%) with the use of cemented sand with a small amount of cement (10% cement content). Yu et al. [21] conducted a series of four-point bending tests on FRP-Concrete-Steel double-skin tubular members with similar dimensions to the specimens in this study (152.5 mm in outer diameter, 1300 mm in span, and 400 mm in shear span). As shown in Table 6, by normalizing the ultimate loads, it can be observed that the new GFRP composite piles exhibit similar flexural capacity to double-skin piles. Moreover, its ultimate deflection is also much higher than that of the double-skin piles (around 150 mm).

2.1.12 Theoretical analysis

According to Yu et al. [21], the traditional section analysis based on the plane section assumption provided a reasonable prediction of the flexure behaviour of the concrete-filled FRP pile. The analysis process included determining the position of the neutral axis for the compressed fibres at a given strain through cross-sectional force equilibrium, and evaluating the bending moment by integrating the contributions of the stresses across the section.

The elastic–perfectly plastic stress–strain curves were adopted for the FRP tubes, and the elastic modulus, tensile strength and compressive strength are listed in Table 1. Due to the significantly lower strength of the cemented sand compared to concrete, the confinement effect coefficient (ξ) of GFRP-confined cemented sand was also considerably lower than that of GFRP-confined concrete. This confinement behaviour was, in fact, more akin to that of steel-confined concrete tubular piles. Consequently, the

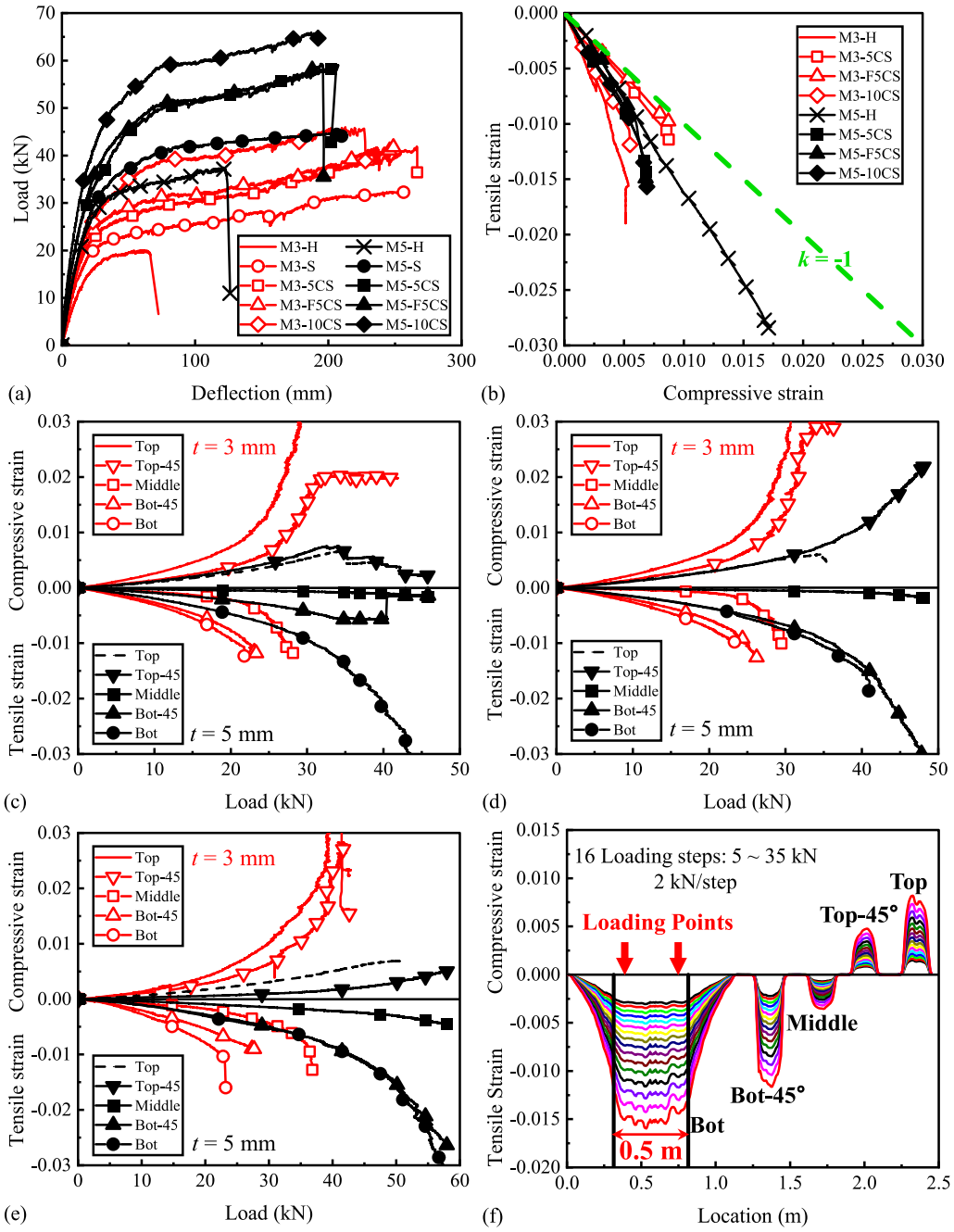

Fig. 12 Test results for GFRP-confined cemented sand piles: **a** Load–deflection relationships; **b** tensile–compressive strain relationships; **c** axial strain distribution for '5CS' piles; **d** axial strain distribution for 'F5CS' piles; **e** axial strain distribution for '10CS' piles; and **f** typical strain profile

following formula proposed by Han [39] was employed to simulate the stress–strain curves of the GFRP-confined cemented sand:

$$\xi = \frac{f_{cu}A_{FRP}}{f_{co}A_c} \tag{1}$$

where A_{FRP} and A_c = cross-sectional area of FRP tube and cemented sand core; f_{cu} = compressive strength of FRP tube.

$$\begin{cases} \sigma_c = f_{co}\left[\dfrac{2\varepsilon_c}{\varepsilon_{co}} - \left(\dfrac{\varepsilon_c}{\varepsilon_{co}}\right)^2\right] & when\ \varepsilon_c \le \varepsilon_{co} \\ \sigma_c = f_{co}\left[1 + \dfrac{\xi^{0.745}}{2+\xi}\cdot\left(\left(\dfrac{\varepsilon_c}{\varepsilon_{co}}\right)^{0.1\xi} - 1\right)\right] & when\ \varepsilon_c > \varepsilon_{co} \end{cases} \tag{2}$$

Table 6 Comparison between the present and previous studies

Comparison	Specimen	Load increment (%)	Normalized moment [M/D^3] (MPa)
Present study	M3-H	-	2.05
	M3-S	61.85	3.31
	M3-5CS	107.25	4.21
	M3-F5CS	108.75	4.28
	M3-10CS	122.90	4.71
FRP-confined concrete [22, 23]	$HP_{3.10}$	-	2.27
	$CP_{3.10}$	160.61	5.93
FRP-Concrete-Steel Double-Skin tubular Members [21]	1F-2.7S-38.2	-	3.07
	2F-2.7S-38.2	-	3.09
	1F-3.2S-38.2	-	2.83
	2F-3.2S-35.5	-	2.99
	1F-4.3S-35.5	-	4.33
	2F-4.3S-35.5	-	4.44

M = moment capacity; D = diameter of the concrete core. The FRP-confined concrete piles were assigned a name, beginning with 'HP' and 'CP' representing the hollow pile and concrete-filled pile, followed by a subscript of '3.10' denoting the shear span/diameter ratio of the pile. The double-skin tubular members were assigned a name, beginning with '1F' or '2F' representing the thickness of the FRP tube (1 ply and 2 plies), followed by '2.7S', '3.2S', or '4.3S', denoting the thickness of the inner steel tube. The last digits '38.2' and '35.5' represent the strength of the concrete between the two tubes

$$\begin{cases} \sigma_t = f_{to}\left[1.2\left(\dfrac{\varepsilon_t}{\varepsilon_{to}}\right) - 0.2\left(\dfrac{\varepsilon_t}{\varepsilon_{to}}\right)^6\right] & when\ \varepsilon_t \le \varepsilon_{to} \\ \sigma_t = f_{to}\left[\dfrac{\left(\frac{\varepsilon_t}{\varepsilon_{to}}\right)}{0.31 f_{to}^2\left(\left(\frac{\varepsilon_t}{\varepsilon_{to}}\right) - 1\right)^2 + \left(\frac{\varepsilon_t}{\varepsilon_{to}}\right)}\right] & when\ \varepsilon_t > \varepsilon_{to} \end{cases} \quad (3)$$

where, f_{co} and ε_{co} = the unconfined cemented sand cylinder strength and the corresponding strain; σ_c and ε_c = the compressive stress and strain of cemented sand; σ_t and ε_t = the tensile stress and strain of cemented sand; $f_{to} = 0.26(1.25f_{co})^{2/3}$ = tensile strength of the unconfined cemented sand; $\varepsilon_{to} = 2f_{to}/E_c$ = corresponding tensile strain.

For each specimen, the maximum compressive strain monitored by the strain gauge was taken as the ultimate point of the stress–strain curve for the GFRP-confined cemented sand pile. For the specimens of sand-filled FRP piles, given the zero cohesion of sand, there was no compressive bearing capacity in an unconfined state. There was a lack of stress–strain models for GFRP-confined granular materials. Therefore, the application of this model for predicting the behaviour of sand-filled FRP piles was not viable.

Figure 13 presents the predicted and experimental load-compressive strain curves for all GFRP-confined cemented sand piles. The strain values represented the maximum compressive strain of the pile at the mid-span. These specimens encompass various FRP tube thicknesses and differing strengths of cemented sand. It can be observed that the theoretical model can reasonably predict the load–strain behaviour of GFRP-confined cemented sand piles. However, for specimens with larger thicknesses (t = 5 mm), certain discrepancies are observed, which may be attributed to sliding between the FRP tube and the concrete due to the increased thickness of the FRP tube (i.e. greater axial rigidity). As a result, the strain recorded on the FRP tube was lower than the predicted value based on the plane section assumption. Indeed, the slip observed during the test of the thicker specimens supports this interpretation. Furthermore, when FRP was combined with weakly cemented materials, its ultimate deformation was significantly greater than the results obtained from material tests [40]. For GFRP-confined sand piles, future research should establish the stress–strain relationships of sand under a range of confining pressures, particularly at high confining pressure levels, to enable prediction of its behaviour under the variable-confinement conditions imposed by a GFRP tube. In practice, the actual loading conditions and boundary conditions of this new pile type differ from those in four-point flexural tests. It is therefore necessary to undertake a series of lateral loading tests and physical model tests in the future study to simulate the behaviour of the pile under realistic field conditions and to provide a solid theoretical basis for its engineering application.

3 Conclusions

This paper has developed a new FRP hybrid system with large ductility and excellent flexural resistance. The new system comprises an external FRP tube and an infill of sand or cemented sand. The new pile allows for extensive, immediate, and facile utilization of sand while reducing the reliance on cement. A series of four-point flexural tests were conducted to validate the expected merits of the new pile and to understand its deformation behaviour and underlying mechanism. The main parameters examined in this study include the thickness of the FRP tube and the

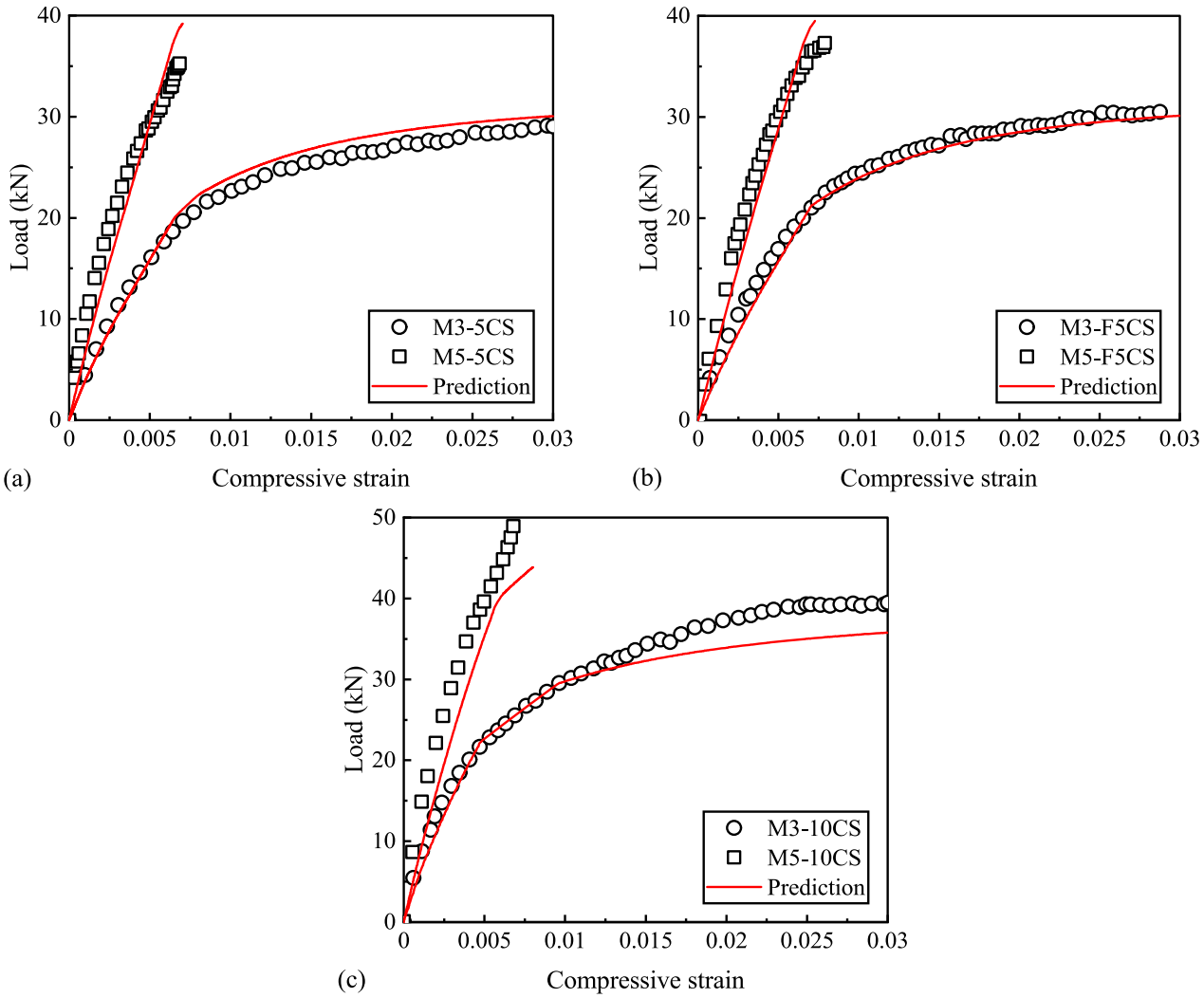

Fig. 13 Comparison of load–compressive strain curves

type of infill material. The results and discussions presented in this study draw the following conclusions:

1. For the sand-filled FRP pile, the sand core could provide internal support for the FRP pile and prevent ovalization and local buckling. Therefore, the ductility of the pile was significantly increased, but the flexural bearing capacity was only slightly improved since the sand core has no tensile strength.
2. The GFRP-confined cemented sand pile demonstrated high levels of both ductility and flexural bearing capacity. With the increase of the cement content of the cemented sand, the stiffness and strength of the cemented sand-filled FRP pile increased. The benefits of incorporating basalt fibres into the cemented sand were less pronounced. Compared to previous studies on GFRP-confined concrete piles, the new GFRP composite piles exhibit satisfactory flexural strength and significantly enhanced deformation capacity.
3. Increasing the thickness of the GFRP tube had a more pronounced impact on the strength of the pile, but it also led to a reduction in the ductility. Additionally, the thicker GFRP tube had a greater axial stiffness, resulting in higher pressures at the loading point after significant deformation and causing a slip between the FRP tube and the cemented sand core.
4. For cemented sand-filled FRP piles, the predictions of the theoretical model demonstrated excellent agreement with the experimental results. Additionally, it is necessary to establish an analytical model to predict the stress–strain behaviour of the sand core.

It is important to mention that most of the existing relevant research on FRP piles focused on GFRP-confined concrete structures, while studies on GFRP-confined granular material and GFRP-confined weakly cementitious materials were limited. Consequently, further experiments

are necessary to verify and ensure the stability of this new structural form.

Acknowledgements This research was financially supported by the Research Grants Council (RGC) of the Hong Kong Special Administrative Region Government (HKSARG) of China (Grant No.: 15217220, R5037-18F, 15210322).

Funding Open access funding provided by The Hong Kong Polytechnic University. University Grants Committee,15217220,Zhen-Yu YIN,R5037-18F,Zhen-Yu YIN,15210322,Wen-Bo Chen

Data availability All data that support the findings of this study are available from the corresponding author upon reasonable request.

Declarations

Conflict of interest We declare that we have no known competing financial interests or personal relationships that could have appeared to influence the work reported in this article.

Ethical approval This is non-human subject research and waived the need for informed consent.

Consent to participate and publish All authors contributed to the study conception and design. All authors read and approved the final manuscript.

References

1. Fam A, Pando M, Filz G, Rizkalla S (2003) Precast piles for route 40 bridge in Virginia using concrete filled FRP tubes. pcij 48:32–45. https://doi.org/10.15554/pcij.05012003.32.45
2. Liang M-T, Lan J-J (2005) Reliability analysis for the existing reinforced concrete pile corrosion of bridge substructure. Cem Concr Res 35:540–550. https://doi.org/10.1016/j.cemconres.2004.05.010
3. Sen R, Mullins G (2007) Application of FRP composites for underwater piles repair. Compos Part B Eng 38:751–758. https://doi.org/10.1016/j.compositesb.2006.07.011
4. Hollaway LC, Leeming M (1999) Strengthening of reinforced concrete structures: using externally-bonded FRP composites in structural and civil engineering. Elsevier
5. Pando MA, Filz GM, Dove JE, Hoppe EJ (2002) Interface shear tests on FRP composite piles. Deep Foundations 2002: An International Perspective on Theory, Design, Construction, and Performance 1486–1500. https://doi.org/10.1061/40601(256)106
6. Anggawidjaja D, Ueda T, Dai J, Nakai H (2006) Deformation capacity of RC piers wrapped by new fiber-reinforced polymer with large fracture strain. Cem Concr Compos 28:914–927. https://doi.org/10.1016/j.cemconcomp.2006.07.011
7. Chen Z-J, Chen W-B, Yin J-H, Malik N (2021) Shaft friction characteristics of two FRP seawater sea-sand concrete piles in a rock socket with or without debris. Int J Geomech. https://doi.org/10.1061/(ASCE)GM.1943-5622.0002059
8. Dai J-G, Bai Y-L, Teng JG (2011) Behavior and modeling of concrete confined with FRP composites of large deformability. J Compos Constr 15:963–973. https://doi.org/10.1061/(ASCE)CC.1943-5614.0000230
9. Guades EJ, Aravinthan T, Islam MM (2010) An overview on the application of FRP composites in piling system. In: Southern Region Engineering Conference 2010. SREC 2010, pp 65–70
10. He H, Chen W, Yin Z-Y, Senetakis K, Yin J-H (2021) A micromechanical-based study on the tribological and creep-relaxation behavior of sand-FRP composite interfaces. Compos Struct 275:114423. https://doi.org/10.1016/j.compstruct.2021.114423
11. Iskander MG, Hassan M (1998) State of the practice review in FRP composite piling. J Compos Constr 2:116–120. https://doi.org/10.1061/(ASCE)1090-0268(1998)2:3(116)
12. Zhang P, Hu R, Zou X, Liu Y, Li Q, Wu G, Ahmed Sheikh S (2021) Experimental study of a novel continuous FRP-UHPC hybrid beam. Compos Struct 261:113329. https://doi.org/10.1016/j.compstruct.2020.113329
13. Zou X, Lin H, Feng P, Bao Y, Wang J (2021) A review on FRP-concrete hybrid sections for bridge applications. Compos Struct 262:113336. https://doi.org/10.1016/j.compstruct.2020.113336
14. Fam AZ, Rizkalla SH (2002) Flexural behavior of concrete-filled fiber-reinforced polymer circular tubes. J Compos Constr 6:123–132. https://doi.org/10.1061/(ASCE)1090-0268(2002)6:2(123)
15. Fam AZYH (2000) Concrete-filled fibre-reinforced polymer tubes for axial and flexural structural members. PhD Thesis, The University of Manitoba
16. Akiyama M, Abe S, Aoki N, Suzuki M (2012) Flexural test of precast high-strength reinforced concrete pile prestressed with unbonded bars arranged at the center of the cross-section. Eng Struct 34:259–270. https://doi.org/10.1016/j.engstruct.2011.09.007
17. Parvathaneni H, Iyer S, Greenwood M (1996) Design and construction of test mooring pile using superprestressing. In: Proceedings of the Advanced Composite Materials in Bridges and Structures (ACMBS). Montreal, Quebec, Canada, pp 313–324
18. Kabir MH, Fawzia S, Chan THT, Badawi M (2016) Durability of CFRP strengthened steel circular hollow section member exposed to sea water. Constr Build Mater 118:216–225. https://doi.org/10.1016/j.conbuildmat.2016.04.087
19. Karbhari V, Seible F, Burgueño R, Davol A, Wernli M, Zhao L (2000) Structural characterization of fiber-reinforced composite short- and medium-span bridge systems. Appl Compos Mater 7:151–182. https://doi.org/10.1023/A:1008974804077
20. Mirmiran A, Shahawy M, Khoury C, Naguib W (2000) Large beam-column tests on concrete-filled composite tubes. ACI Struct J 97:268–276
21. Yu T, Wong YL, Teng JG, Dong SL, Lam ES (2006) Flexural behavior of hybrid FRP-concrete-steel double-skin tubular members. J Compos Constr 10:443–452. https://doi.org/10.1061/(ASCE)1090-0268(2006)10:5(443)
22. Ferdous W, Almutairi AD, Huang Y, Bai Y (2018) Short-term flexural behaviour of concrete filled pultruded GFRP cellular and tubular sections with pin-eye connections for modular retaining wall construction. Compos Struct 206:1–10. https://doi.org/10.1016/j.compstruct.2018.08.025
23. Ferdous W, Bai Y, Almutairi AD, Satasivam S, Jeske J (2018) Modular assembly of water-retaining walls using GFRP hollow

profiles: components and connection performance. Compos Struct 194:1–11. https://doi.org/10.1016/j.compstruct.2018.03.074
24. Ashpiz ES, Egorov AO, Ushakov AE (2010) Application of composite materials for the protection of sea shores and engineering structures against the impact of waves. Brac Croatia, pp 231–238
25. Teng J-C, Yin Z-Y, Chen W-B, Song D-B, Dai J-G (2024) Interface shear behavior of sandy soil-FRP with epoxy hardness effect and abrasion. J Compos Constr 28:04024064. https://doi.org/10.1061/JCCOF2.CCENG-4707
26. Teng J-C, Yin Z-Y, Song D-B, Jin Y-F, Chen W-B, Dai J-G (2025) Utilization of sand-filled FRP tubular pile retaining wall with sand back fill adjacent to strip footing: model study. Acta Geotech. https://doi.org/10.1007/s11440-025-02574-2
27. Cao S, Xue G, Yilmaz E (2019) Flexural behavior of fiber reinforced cemented tailings backfill under three-point bending. IEEE Access 7:139317–139328. https://doi.org/10.1109/ACCESS.2019.2943479
28. Xue G, Yilmaz E, Feng G, Cao S (2021) Bending behavior and failure mode of cemented tailings backfill composites incorporating different fibers for sustainable construction. Constr Build Mater 289:123163. https://doi.org/10.1016/j.conbuildmat.2021.123163
29. Yu T, Zhao H, Ren T, Remennikov A (2019) Novel hybrid FRP tubular columns with large deformation capacity: concept and behaviour. Compos Struct 212:500–512. https://doi.org/10.1016/j.compstruct.2019.01.055
30. Zhao H, Ren T, Remennikov A (2021) Behaviour of FRP-confined coal rejects based backfill material under compression. Constr Build Mater 268:121171. https://doi.org/10.1016/j.conbuildmat.2020.121171
31. Teng J-C, Yin Z-Y, Chen W-B, Song D-B, Dai J-G (2024) Behavior of FRP-confined sand and cemented sand under axial compression. J Mater Civ Eng 36:04024433. https://doi.org/10.1061/JMCEE7.MTENG-18403
32. ASTM (2017) Standard test method for tensile properties of polymer matrix composite materials. ASTM D3039 ASTM Committee D30
33. GB/T (2005) Fiber-reinforced thermosetting plastic composites pipe - Determination for longitudinal compressive properties. GB/T 5350–2005 China national standardization management committee. 2005. Beijing; China.
34. ASTM (2017) Standard practice for classification of soils for engineering purposes (unified soil classification system). ASTM D2487 West Conshohocken, PA: ASTM
35. Consoli NC, Cruz RC, Floss MF, Festugato L (2010) Parameters controlling tensile and compressive strength of artificially cemented sand. J Geotech Geoenviron Eng 136:759–763. https://doi.org/10.1061/(ASCE)GT.1943-5606.0000278
36. BSA (1980) Mortar and concrete–test method for compressive strength of cylindrical specimens. NBR 5739 BRAZILIAN STANDARD ASSOCIATION
37. Lv C, Zhu C, Tang C-S, Cheng Q, Yin L-Y, Shi B (2021) Effect of fiber reinforcement on the mechanical behavior of bio-cemented sand. Geosynth Int 28:195–205. https://doi.org/10.1680/jgein.20.00037
38. Xiao Y, He X, Evans T, Stuedlein A, Liu H (2019) Unconfined compressive and splitting tensile strength of basalt fiber-reinforced biocemented sand. J Geotech Geoenviron Eng 145:04019048. https://doi.org/10.1061/(ASCE)GT.1943-5606.0002108
39. Han L (2016) Concrete filled steel tubular structures from theory to practice. CHINA SCIENCE PUBLISHING & MEDIA LTD
40. Teng J (2024) Behaviour and modelling of sand-filled GFRP pile-wall system in reclamation engineering. PhD Thesis, The Hong Kong Polytechnic University